Journal of Colloid and Interface Science 689 (2025) 137245

Contents lists available at ScienceDirect

Journal of Colloid And Interface Science

journal homepage: www.elsevier.com/locate/jcis

Regular Article

N,S-doped Ti_3C_2 MXene quantum dots-anchored metal ruthenium: Efficient electrocatalyst for pH-universal hydrogen evolution reaction

Lan Ding [a,*], Jing Xu [a], Zeyu Zhang [a], Kezhen Qi [a,*], Ge Jin [b,*]

[a] College of Pharmacy, Dali University, Dali 671000, China
[b] School of Chinese Medicine, Shenyang Medical College, Shenyang 110034 Liaoning, China

GRAPHICAL ABSTRACT

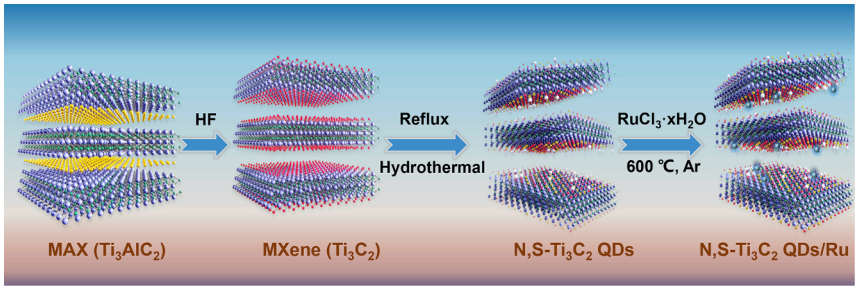

ARTICLE INFO

Keywords:
Hydrogen evolution reaction
N,S-doped Ti_3C_2 QDs
Ruthenium (Ru)
Electronic interaction
pH-universal

ABSTRACT

Electrocatalytic hydrogen evolution reaction (HER) via water splitting is a prospective technology for achieving the sustainable production of hydrogen. So, ruthenium-based electrocatalysts have been extensively studied. However, metallic ruthenium tends to agglomerate due to the high cohesive energy, resulting in decreased HER performance in practical usage. Introducing sufficient support for dispersing and immobilizing ruthenium-based species is a viable way to enhance the utilization efficiency. MXene-based materials with unique surface termination groups, superior chemical stability, high specific surface area and favorable electrical conductivity have received significant attention as low-cost carriers for the development of active catalysts in HER. Herein, nitrogen (N) and sulfur (S) atom-doped titanium carbide (Ti_3C_2) quantum dots (QDs) were successfully synthesized as efficient carriers for anchoring ultra-small ruthenium nanoparticles (NPs) toward electrocatalytic HER. Electrochemical tests reveal that the resultant N,S-Ti_3C_2 QDs/Ru displays superior HER performance with low overpotentials of 28, 25 and 56 mV at 10 mA cm^{-2} current density in 0.5 M H_2SO_4, 1 M KOH and 1 M PBS solutions, respectively. Such a low overpotential is comparable to most previously reported non-metallic catalysts, Ru-based electrocatalysts and commercial Pt/C. In addition, N,S-Ti_3C_2 QDs/Ru displays extraordinarily long-term stability over a relatively wide pH range and is indeed a kind of pH-universal catalyst for hydrogen evolution. Furthermore, density functional theory (DFT) calculations demonstrate that the interactions between metal Ru and N,S-Ti_3C_2 MXene QDs effectively regulate the electronic structure of the active site Ru, lowering the energy barrier of the electrocatalytic HER intermediate, thus dramatically enhancing the activity for N,S-Ti_3C_2 QDs/Ru. This work proposes a novel approach to functionalize MXene quantum dots for use as low-cost electrocatalysts with promising practical applications in renewable energy conversion.

* Corresponding authors.
E-mail addresses: 15030527652@163.com (L. Ding), qkzh2003@aliyun.com (K. Qi), iecd@symc.edu.cn (G. Jin).

https://doi.org/10.1016/j.jcis.2025.03.034
Received 30 December 2024; Received in revised form 2 March 2025; Accepted 3 March 2025
Available online 4 March 2025

1. Introduction

With the fast development of society, the massive depletion of fossil fuels has resulted in serious energy and environmental crises, which urgently require in-depth and systematic research into the exploration of sustainable energy sources [1–3]. Owing to the limitation of resources of wind, tide and solar energy, hydrogen (H_2) is considered as a prospective replacement for classical fossil fuels by virtue of its high energy density, renewability and abundant resources [4–7]. Electrocatalytic water splitting is regarded as the tremendously prospective approach for the economical and efficient production of hydrogen fuel [8–10]. Currently, noble metal platinum based materials represent the state-of-the-art electrocatalysts for HER ascribed to the close-to-zero hydrogen-absorbing Gibbs free energy (ΔGH*), which remarkably diminishes the kinetic barriers and enhances the electrocatalytic process rate [11,12]. In fact, the large-scale practical industrial applications for Pt-based electrocatalytic materials are extremely restricted by the high cost and scarcity of Pt [13]. Thus, the exploitation of high efficiency, stable and low-cost electrocatalysts is a paramount importance in the roadmap of electrolytic water. As a member of platinum-group metals, metallic Ru possesses a low cost (about 5 % of Pt). Moreover, the binding strength to hydrogen is comparable with Pt (≈65 kcal mol^{-1}), making it regarded as an appealing alternative to Pt for catalyzing the HER [14–16]. Nevertheless, Ru NPs tend to aggregate owing to the high cohesive energy, resulting in reduced HER activities during practical electrochemical reactions [17,18]. Appropriate improvement strategies also require to be explored for the further boost of the HER performance of ruthenium-based electrocatalysts. The construction of suitable carrier materials can efficiently stabilize the nanoparticles of metallic Ru, which is crucial for optimizing dispersion, decreasing particle size, and augmenting the density of active sites and cycling durability [19–21]. Additionally, the strong interfacial coupling effect between metal Ru and the carrier will cause the redistribution of charge density, thus altering the surface adsorption and lowering the reaction energy barriers. To this end, numerous carrier materials, including graphene nanosheets, carbon nanotubes, carbon dots and metal oxides have been widely employed for the effective design and synthesis of high-performance Ru-based composite catalysts [22–25]. Unfortunately, those materials tend to have electrochemically inert, undesirable conductors and hydrophobic properties. Despite several research advances, developing low-cost supports with superior electrical conductivity, electrochemical activity and hydrophilicity for the large-scale fabrication of highly efficient and robust HER electrocatalysts remains unrealized.

As an emergent class of two-dimensional (2D) materials, MXenes have been arousing tremendous research interest owing to their superior physicochemical properties [26–28]. Under this context, the MXene QDs, especially derived from MXene, featuring a small size of less than 10 nm, inherit the unusual physicochemical advantages of bulk MXene, such as excellent electronic conductivity with efficient charge transport, affluent surface termination groups, excellent surface activities, and hydrophilic functional groups, large surface specific area, thus offering abundant active basal and edge active sites. These fascinating properties make MXene QDs attractive for various potential applications, including supercapacitors, energy storage, Li-sulfur batteries, solar cells, and photo/electrocatalysts [29,30]. Notably, the size reduction of MXene to <10 nm can promote rapid electron transfer to the electrochemically active site, thereby improving the charge transfer kinetics. Recent DFT further suggests that the ΔGH* on the oxygen terminus in MXenes is close to the optimal value (0 eV), which plays a vital role for HER [31,32]. The high specific surface area of MXene QDs can restrict metal Ru atoms between MXene QDs to form structurally stable ultrafine nanocrystals, preventing the agglomeration and growth of metal nanoparticles. In particular, the superior electrical conductivity and abundant surface functional groups (—COOH, —NH_2, —OH) of MXene QDs endow more binding sites with metals, thus providing more possibilities for the modulation of electronic structure and hydrogen production performance of the catalysts [33,34]. Moreover, as reported in previous research, according to the discrepancy of electron spin density and electronegativity among the metals and heteroatoms, introducing additional electronegative heteroatom (such as N, S, P) coordination in MXene QDs can effectively regulate the charge structure, optimize the intermediate adsorption, realizing the improvement of catalytic activity [35,36]. Consequently, MXene QDs may be an ideal support for the preparation of metal Ru-based HER composite electrocatalysts.

Herein, we developed N and S doped Ti_3C_2 MXene QDs as an effective solid support for anchoring ultrafine Ru NPs via simple hydrothermal and pyrolysis approaches. The Ru NPs are stabilized on the functionalized N,S-Ti_3C_2 QDs support through forming Ru-N and Ru-S bonds with N and S, thus inhibiting their aggregation and growth. Remarkably, the as-prepared N,S-Ti_3C_2 QDs/Ru electrocatalyst presents favorable HER activity with an extremely low overpotential of 28, 25, and 56 mV at 10 mA cm^{-2} current densities in acidic, alkaline and neutral solutions, respectively, which are superior to the most previous Ru-based catalysts. Moreover, the N,S-Ti_3C_2 QDs/Ru displays significantly improved long-term stability across a relatively wide pH range. DFT calculations indicate that the coordination interactions between Ru and N,S-Ti_3C_2 QDs efficiently adjust the electronic structure in the active site Ru, lower the energy barrier of the intermediates in HER reaction, and realize the optimal ΔGH* of hydrogen adsorption. This work can be extended to other MXene materials for the reasonable construction of high-efficiency catalysts and provide a new perspective for enhancing the performance of the electrocatalysts.

2. Experimental section

2.1. Materials

Ti_3AlC_2 phase (98.0 %) was purchased from Aladdin. Concentrated nitric acid (HNO_3, 68.0 %) and concentrated sulfuric acid (H_2SO_4, 98.0 %) were purchased from Shanghai Macklin Biochemical Technology Co., Ltd. Ruthenium Chloride hydrate ($RuCl_3{\cdot}xH_2O$) and thiourea (CH_4N_2S, 98.0 %) were purchased from Shanghai Haohong Biopharmaceutical Technology Co Ltd. Hydrofluoric acid (HF, 40.0 %) was purchased from Sigma-Aldrich.

2.2. Synthesis of N and S doped Ti_3C_2 QDs

1 g of Ti_3AlC_2 MAX phase was slowly dissolved in 25 mL of HF solution. Then, the solution was kept at 50°C while continuously stirring in an oil bath for 72 h. The powder products were washed three times with distilled water and centrifuged at 4000 rpm for 2 min each time. The resultant powder was mixed with 45 mL of deionized water and ultrasonicated over 60 min. After separation, the multilayered Ti_3C_2 MXene deposit was collected for freeze-drying and used for subsequent experiments later. The N and S doped Ti_3C_2 QDs were prepared by a facile acid reflux-assisted hydrothermal method: The obtained multilayered Ti_3C_2 MXene was distributed in the mixture with H_2SO_4 and HNO_3 solutions and reacted thoroughly at 100 °C over 12 h. The appropriate amount of NaOH was slowly added into the above solution to moderate the pH up to 6–7, obtaining the MXene solution with sizeable small flakes of MXene. Subsequently, 0.1g of thiourea was dissolved in a solution that contained 15 mL of the above solution and 3 mL of distilled water was stirred magnetically and then removed to the Teflon autoclave and kept at 160 °C for 12 h. Eventually, the reaction solution was transferred to a dialysis bag to purify the N,S-Ti_3C_2 QDs, and the final product N,S-Ti_3C_2 QDs powder was obtained via freeze-drying and collected for the further use.

2.3. Synthesis of Ru NPs

10.0 mL of $RuCl_3$ aqueous solution (10 mg/mL) was gradually added to 30 mL of deionized water and stirred thoroughly at room temperature

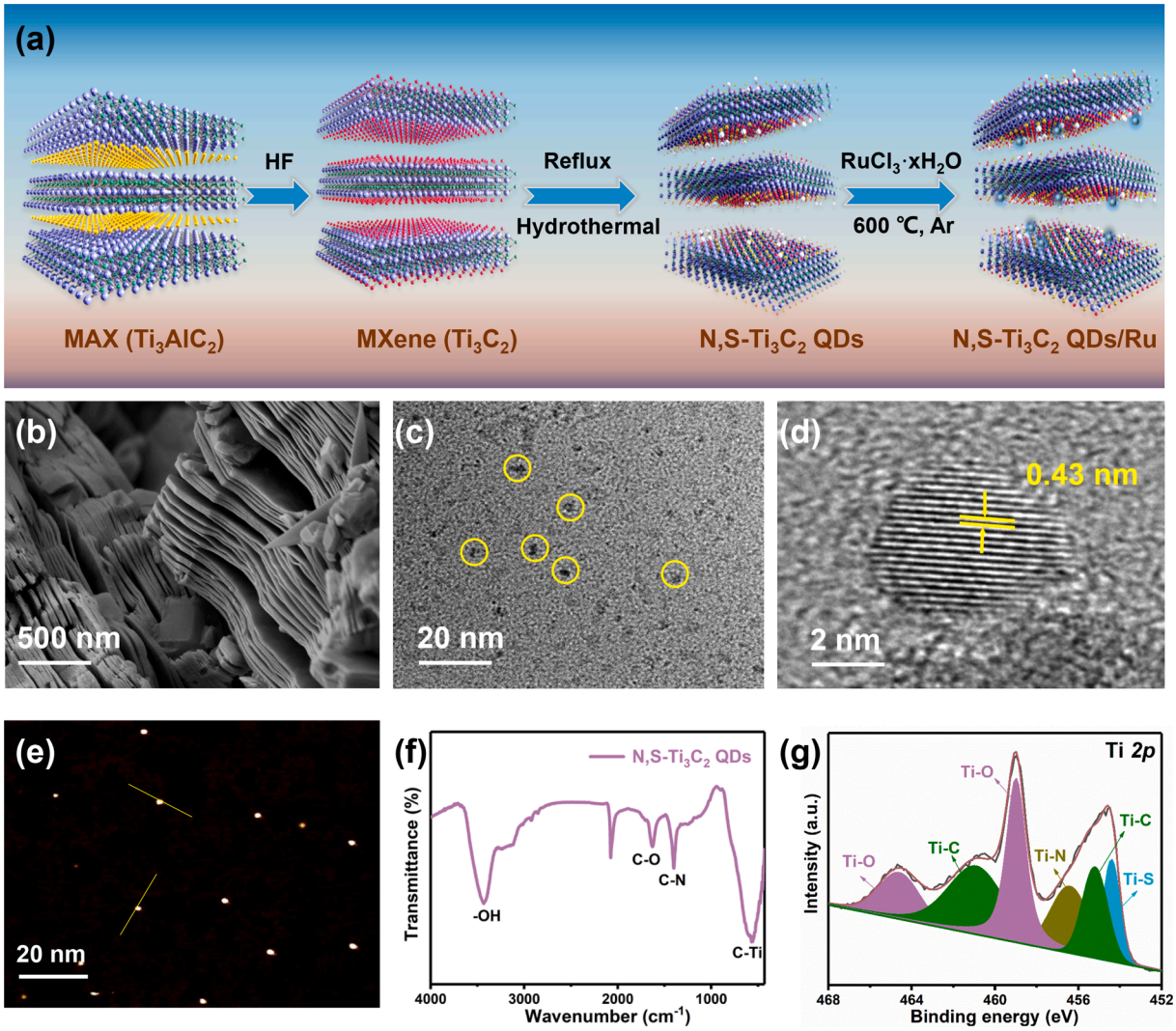

Fig. 1. (a) Schematic diagram of the preparation for N,S-Ti_3C_2 QDs/Ru electrocatalyst, (b) SEM image for Ti_3C_2 MXene, (c, d) TEM and HRTEM images for N,S-Ti_3C_2 QDs, (e) AFM image for N,S-Ti_3C_2 QDs, (f) FT-IR spectra for N,S-Ti_3C_2 QDs, (g) Ti 2p XPS spectra for N,S-Ti_3C_2 QDs.

for 2 h. After vacuum drying, the resultant powder was placed into a tube furnace and calcined under an Ar atmosphere at 600 °C for 5 h using a heating rate of 5 °C/min, and the product was marked as Ru NPs.

2.4. Synthesis of N,S-Ti_3C_2 QDs/Ru

50 mg of N,S-Ti3C2 QDs were dispersed into 30 mL of distilled water with vigorous sonication. Then, 10 mL of $RuCl_3$ aqueous solution (10 mg/mL) was gradually mixed into the as-prepared suspension and stirred thoroughly for 45 min. After freeze-drying, the resultant powder was deposited into a tube furnace and calcined at 500, 600, 700, and 800 °C under the Ar atmosphere for 5 h using a heating rate of 5 °C/min, and the obtained products were marked as N,S-Ti_3C_2 QDs/Ru-500, N,S-Ti_3C_2 QDs/Ru-600, N,S-Ti_3C_2 QDs/Ru-700, and N,S-Ti_3C_2 QDs/Ru-800, respectively. To further analyze the impact of different Ru contents on their HER performance, the 10 mL of $RuCl_3$ aqueous solution (10 mg/mL) was replaced with 1, 3, 5, 7 and 9 mL, respectively, and the corresponding electrocatalysts were marked as N,S-Ti_3C_2 QDs/Ru-X, where X stands for 1, 3, 5, 7, 9.

2.5. Electrochemical measurements

Electrochemical measurements were evaluated at the CHI 760E electrochemical workstation with a traditional three-electrode assembly. KOH solution (1.0 M), H_2SO_4 solution (0.5 M) and PBS solution (1.0 M) were applied as electrolytes, respectively. The as-prepared electrocatalysts were used as working electrodes and graphite rods as counter electrodes. Notably, the Ag/AgCl electrode was employed as the reference electrode in H_2SO_4 solution and the saturated calomel electrode was taken as the reference electrode in KOH and PBS electrolytes. In addition, the working electrodes were treated as follows: 10 mg of electrocatalysts and 60 μL of 5 wt% Nafion solution was mixed into 940 μL of anhydrous ethanol and continuously sonicated over 15 min. Subsequently, the catalyst slurry was evenly coated on the carbon cloth and dried in a vacuum oven with 30 min. The linear sweep voltammetry (LSV) curves of samples were measured under 0.5 M H_2SO_4, 1 M KOH and 1 M PBS solution, respectively with a sweep rate of 5 mV/s. The Tafel plots of catalysts were obtained from the corresponding linear regions of overpotential versus the logarithm of the current density following the Tafel equation as follows:

$$\eta = \mathbf{b}\log|j| + \mathbf{a}$$

The η, j, b, and a in the above equation denote the corresponding overpotential, current densities, Tafel slope and intercept, respectively. To investigate the stability of the catalyst, a continuous 5000 cyclic voltammetry (CV) scan experiment was conducted over the range of 0.1–0.4 V at a scan rate of 10 mV s^{-1}. The long-term HER stability experiments were further studied under the specified current density of 10

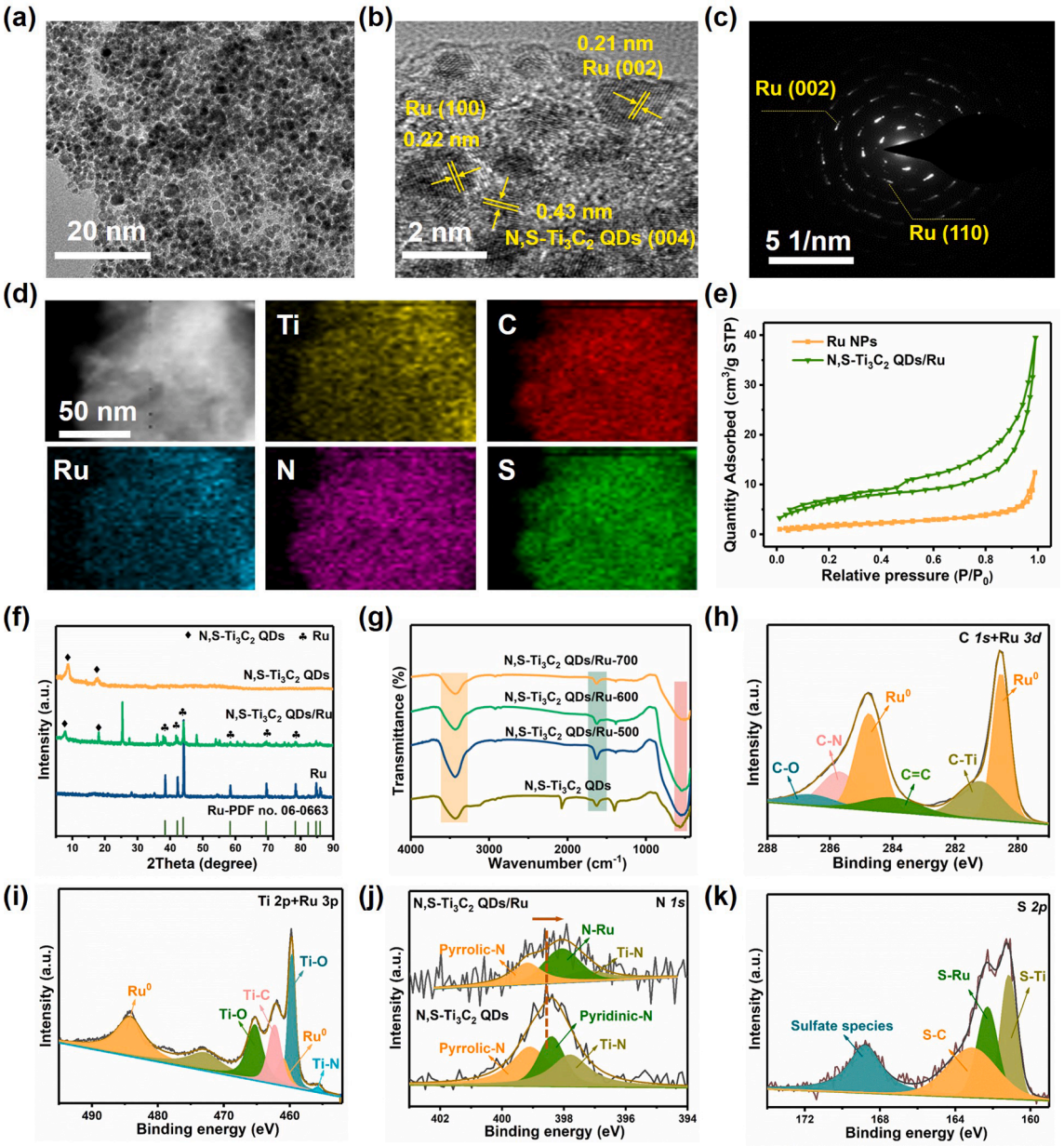

Fig. 2. (a, b) TEM and HRTEM images for N,S-Ti_3C_2 QDs/Ru, (c) SEAD pattern recorded from the corresponding area of N,S-Ti_3C_2 QDs/Ru, (d) Element mapping of N,S-Ti_3C_2 QDs/Ru, (e) N_2 adsorption–desorption isotherms of Ru and N,S-Ti_3C_2 QDs/Ru, (f) XRD pattern of N,S-Ti_3C_2 QDs, Ru and N,S-Ti_3C_2 QDs/Ru, (g) FT-IR spectra for N,S-Ti_3C_2 QDs and N,S-Ti_3C_2 QDs/Ru, (h) C 1 s and Ru 3d XPS spectra of N,S-Ti_3C_2 QDs/Ru, (i) Ti 2p and Ru 3p XPS spectra for N,S-Ti_3C_2 QDs/Ru, (j) N 1 s XPS spectra for N,S-Ti_3C_2 QDs and N,S-Ti_3C_2 QDs/Ru, (k) S 2p XPS spectra for N,S-Ti_3C_2 QDs/Ru.

mA cm^{-2} over 24 h. The impedance spectra (EIS) were measured over a frequency range between 10^5 and 0.01 Hz, and under a peak-to-peak sinusoidal potential perturbation of 10 mV. To study the electrochemical active surface area (ECSA) of synthesized catalysts, a series of CV curves were recorded under various scan rates (namely, 50, 100, 150, 200, 250 and 300 mV s^{-1}). The ECSA was calculated as:

$$ECSA = \frac{C_{dl}(mFcm^{-2})}{40\mu Fcm^{-2}percm^{2}_{ECSA}}$$

2.6. Characterization

X-ray diffraction (XRD) patterns of the catalysts were analyzed with the Bruker D8 Advance using Cu Ka irradiation. The scanning electron microscope (SEM) and energy dispersive X-ray spectroscopy (EDS) images were obtained utilizing Hitachi-S4800 scanning electron microscopy. A Tecnai F20 (FEI) field emission transmission electron microscope was employed to observe the morphology and microstructure under an acceleration voltage of 200 kV. X-ray photoelectron spectroscopy (XPS) analysis results were performed on the Thermo scalable 250xi photoelectron spectroscope instrument. The thickness of the MXene QDs were measured on the Atomic force microscopy (AFM) with a Bruker Dimension. The content of metal Ru was determined by the inductively coupled plasma optical emission spectrometry (ICP-OES) (Agilent 5110 spectrometer). The Fourier transformed infrared (FTIR) spectra of the catalysts were characterized with a Nicolet IS10 spectrometer (Thermo Nicolet Corporation), using KBr as diluent. The BET surface area of the synthesized catalysts was evaluated on an ASAP 2460 system (Micromeritics Instrument) by nitrogen adsorption–desorption isotherms.

2.7. DFT calculation

All DFT computations were performed with the Vienna ab initio simulation package (VASP). The surface structure of Ru consists of 72 Ru atoms, and the lattice parameters of this structure are α = 90°, β = 90°, γ = 120°, with lattice constants a = 8.12 Å, b = 8.12 Å, and c = 36.60 Å. The structure of Ti_3C_2 contains 135 atoms, of which 81 Ti atoms and 54C atoms. The lattice parameters are as follows: the interplanar angles are α = 90°, β = 90°, and γ = 120°, with lattice constants a = 9.20 Å, b = 9.20 Å, and c = 36.60 Å. Based on the experimentally measured atom ratios, N and S atoms were introduced to construct the N,S-Ti_3C_2 QDs model. Subsequently, the N,S-Ti_3C_2 QDs/Ru model was constructed by adding four Ru atoms to the surface. The generalized gradient approximation (GGA) and PBE generalization (Perdew-Burke-Ernzerhof generalization) were used to calculate the exchange–correlation energies, and the projected augmented wave (PAW) was employed to depict the electron–ion interactions. The energy cutoff for the plane wave unfolding was set to 450 eV, and the convergence thresholds were established at 10^{-5} eV in energy and 0.03 eV $Å^{-1}$ in force, respectively. For the calculations of the flat plate model, a vacuum space of 10 Å was added to escape the interaction between periodic images.

3. Results and discussion

A diagram representing the synthesis route for the N,S-Ti_3C_2 QDs/Ru electrocatalyst is presented in Fig. 1a. The layered Ti_3C_2 MXene was fabricated via selective etching of the Al layer of the Ti_3AlC_2 MAX phase with HF. Subsequently, N and S-doped Ti_3C_2 QDs were obtained via a simple reflux-hydrothermal procedure with thiourea. To synthesize the N,S-Ti_3C_2 QDs/Ru electrocatalyst, the as-prepared N,S-Ti_3C_2 QDs were mixed with $RuCl_3{\cdot}xH_2O$ in an aqueous solution and then freeze-dried. The enriched surface functional groups (—F, —O, and —OH) on the N, S-Ti_3C_2 QDs surface tend to interact or adsorb with the Ru^{3+} ions, thus facilitating the binding of Ru on the N,S-Ti_3C_2 QDs support. Furthermore, the freeze-drying process can significantly inhibit the agglomeration of N,S-Ti_3C_2 QDs, which contributes to the uniform dispersion of Ru metal on the carrier. The resulting powder was calcined under 600 °C in the Ar atmosphere, and the ultrafine Ru NPs were successfully doped on N,S-Ti_3C_2 QDs, resulting in the formation of N,S-Ti_3C_2 QDs/Ru. The SEM image shows a regular accordion-like structure, indicating that Ti_3C_2 MXene was successfully prepared by HF etching (Fig. 1b). The element mapping image of Ti_3C_2 MXene indicates that the evenly dispersion of Ti and C elements (Fig. S1). The microstructure of N,S-Ti_3C_2 QDs was characterized via transmission electron microscopy (TEM). Apparently, the N,S-Ti_3C_2 QDs possess excellent dispersion (Fig. 1c) with an average diameter of 4.4 nm (Fig. S2). The distinct lattice fringes can be further noticed from the HRTEM image of N,S-Ti_3C_2 QDs, and the lattice spacing about 0.43 nm assigned to the (004) facet of Ti_3C_2 MXene (Fig. 1d). The AFM characterization displays a thickness of the N,S-Ti_3C_2 QDs ranges from 1.0 to 2.2 nm, which suggests that the majority of N,S-Ti_3C_2 QDs corresponds to monolayer QDs (Fig. 1e and Fig. S3). FTIR spectra was conducted to analyze the surface groups for N,S-Ti_3C_2 QDs sample (Fig. 1f). FTIR spectra shows that N,S-Ti_3C_2 QDs are rich in functional groups, and the stretching vibrations at about 620, 1407, 1650, and 3420 cm^{-1} are induced by Ti—C, C—N, C—O, and —OH bonds, respectively, which promote the anchoring of Ru NPs. The XPS survey spectra for N,S-Ti_3C_2 QDs (Fig. S4) show the appearance of C, Ti, N and S elements, confirming the successful fabrication of N and S atoms co-doped Ti_3C_2 QDs. The C 1s XPS spectra for N, S-Ti_3C_2 QDs exhibit characteristic peaks at 281.4, 283.8, 284.9 and 288.4 eV (Fig. S5), which belong to C—Ti, C—N, C—C, and C═O, respectively. The presence of C-Ti proves that N,S-Ti_3C_2 QDs still retain the lamellar structure of the two-dimensional Ti_3C_2 MXene. Fig. 1g shows the Ti 2p XPS spectra of N,S-Ti_3C_2 QDs, the peaks in 454.4 eV and 461.1 eV correspond to Ti-C, which further confirms that the well-preserved planar structure of Ti_3C_2. Meanwhile, the peaks in 458.9 eV and 464.6 eV ascribed to Ti—O bonds, resulting from the formation of surface oxygen-containing functional groups in the etching process. The peaks appearing in 456.4 eV and 454.4 eV are belong to Ti-N and Ti-S, further evidencing the successful doping of N and S atoms [37,38].

The morphology and structures of samples were studied by TEM. The pure Ru NPs appear to have obvious agglomeration due to the higher surface energy (Fig. S6). In contrast, the N,S-Ti_3C_2 QDs/Ru show a thin sheet structure loaded with massive nanoparticles, and the Ru NPs are homogeneously anchored on the N,S-doped Ti_3C_2 QDs support (Fig. 2a). The loaded Ru NPs possess a small particle size, indicating that N,S-Ti_3C_2 QDs as suitable supports significantly inhibited the aggregation and growth of Ru. Furthermore, the HRTEM indicates the lattice fringes with 0.21 nm and 0.22 nm match the (002) and (100) facets of metal Ru, respectively, and the lattice fringe of 0.43 nm matched the (004) facets for N,S-Ti_3C_2 QDs, revealing the high crystallinity of N,S-Ti_3C_2 QDs/Ru (Fig. 2b). The existence of diffraction rings corresponding to the (002) and (110) faces of Ru in the SAED image of N,S-Ti_3C_2 QDs/Ru reconfirms the existence of Ru NPs (Fig. 2c). The elemental mapping further suggests that C, N, S, Ti and Ru are uniformly dispersed in N,S-Ti_3C_2 QDs/Ru (Fig. 2d). Moreover, the ICP test demonstrates that the content of Ru in the composites is 1.8 wt%. Fig. 2e shows the N_2 adsorption–desorption isotherms of Ru and N,S-Ti_3C_2 QDs/Ru. The specific surface area of as-prepared N,S-Ti_3C_2 QDs/Ru is 124.5 m^2/g, which is much higher than 31.6 m^2/g of pure Ru NPs (Fig. S7), suggesting that the introduction of N,S-Ti_3C_2 QDs support facilitates the dispersion of metal Ru, thus promoting the exposure of more reactive sites. To explore the crystallization process, N,S-Ti_3C_2 QDs/Ru samples were prepared under different annealing temperatures. As illustrated in Fig. S8, when the calcination temperature is 500 °C, minority Ru NPs are noticed to begin appearing in lattice fringes. While the calcination temperature is at 700 °C and 800 °C, the Ru NPs obviously grew and aggregated, thus decreasing the efficient exposure area of the catalyst and inhibiting the catalytic reaction. These findings suggest that with the increasing calcination temperature, the crystallinity and particle size of Ru NPs gradually enhanced. Besides, the excessively high temperature is not favorable for the distribution of Ru NPs. The crystal structures of the prepared catalysts were examined through XRD. As illustrated in Fig. S9, the pristine Ti_3AlC_2 exhibits distinct diffraction peaks, and the vital diffraction peak at 39° disappears after etching with HF solution, demonstrating that the Al layer has been completely removed. The widening of the interlayer spacing of the synthesized Ti_3C_2 MXene resulted in the weakening of the intensity of the characteristic peak (002) and shifting to a lower position [39]. Moreover, the (002) and (004) crystal planes of the layered structured Ti_3C_2 MXene can still be observed in the N,S-Ti_3C_2 QDs, which suggests that the prepared N,S-Ti_3C_2 QDs still retain partial chemical properties of pristine MXene, which is consistent with the HRTEM results of N,S-Ti_3C_2 QDs. As illustrated in Fig. 2f, the characteristic diffraction peaks for pure Ru occurring at 38.3°, 42.1°, 44.0°, 58.3°, 69.4° and 78.3° belong to the (100), (002), (101), (102), (110) and (103) crystal planes of metallic Ru (Ru^0) with hcp crystalline structure (JCPDS 06-0663), respectively [40]. N,S-Ti_3C_2 QDs/Ru exhibits the characteristic peaks at 7.8° and 18.4°, which can be ascribed to the (002) and (004) planes of the N,S-Ti_3C_2 MXene QDs, and the diffraction peaks at 42.1°and 44.0° of N,S-Ti_3C_2 QDs/Ru belong to the (002) and (101) planes of metallic Ru, which demonstrates the Ru NPs are successfully anchored on the N,S-Ti_3C_2 MXene QDs support. Additionally, the characteristic diffraction peaks appearing at 25° for the N,S-Ti_3C_2 QDs/Ru composites can be attributed to the formation of a small amount of RuO_2 phases during the high temperature calcination process. Whereas the weak diffraction peak observed at 47° corresponds to the (200) crystallographic diffraction of the face-centered cubic (fcc) structured metal Ru, which may be attributed to the substable phase transition due to the nanoscale effect of Ru [41,42]. Fig. S10 shows the XRD patterns of N,S-Ti_3C_2 QDs/Ru synthesized at various calcination temperatures. The weak diffraction peak of Ru was observed at 500 °C calcination temperature, indicating that the N,S-

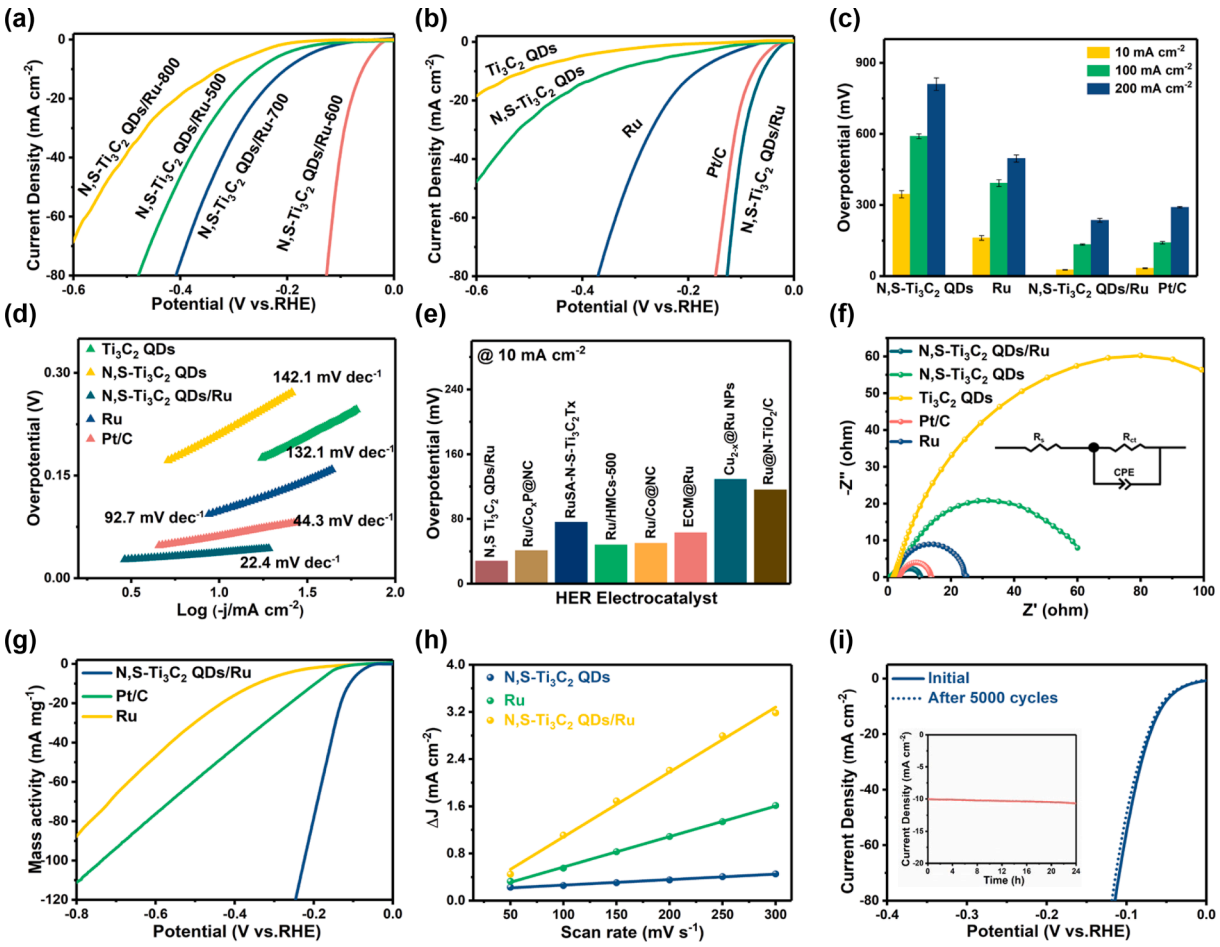

Fig. 3. (a) LSV curves of N,S-Ti_3C_2 QDs/Ru catalyst at different calcination temperatures, (b) LSV curves of various catalysts, (c) overpotentials in 10, 100 and 200 mA cm^{-2} current density (error bars represent the standard deviation of three independent measurements), (d) Corresponding Tafel slopes, (e) The comparison of HER performance of Ru-based electrocatalysts in 0.5 M H_2SO_4, (f) EIS spectra of various catalyst, (g) mass activity of Pt/C, Ru and N,S-Ti_3C_2 QDs/Ru, (h) Double-layer capacitance (C_{dl}) plots of Ru, N,S-Ti_3C_2 QDs and N,S-Ti_3C_2 QDs/Ru, (i) LSV curves for N,S-Ti_3C_2 QDs/Ru before and after 5000 CV cycles. The inset shows the current density-time curve for N,S-Ti_3C_2 QDs/Ru during the HER process.

Ti_3C_2 QDs/Ru is poorly crystallized. When the calcination temperature reaches above 600 °C, the sharp Ru diffraction peaks appear in N,S-Ti_3C_2 QDs/Ru, indicating that the Ru NPs are fully crystallized. The FTIR spectra are shown in Fig. 2g, the N,S-Ti_3C_2 QDs/Ru demonstrates similar stretching vibrations, suggesting that the surface functional groups can be well preserved in N,S-Ti_3C_2 QDs/Ru, and the loading of Ru has not damaged the backbone structure of the quantum dots in N,S-Ti_3C_2 QDs [43]. XPS analysis was utilized to further ascertain the surface chemical states and electronic interactions of N,S-Ti_3C_2 QDs/Ru. Fig. 2h exhibits the C 1s and Ru 3d XPS spectra for N,S-Ti_3C_2 QDs/Ru. The binding energy peaks of 286.7, 285.7, 283.8 and 281.2 eV belong to C—O, C—N, C═C, and C—Ti, respectively [44,45]. Moreover, the additional peak observed for N,S-Ti_3C_2 QDs/Ru at 280.4 eV and 284.7 eV can be assigned to Ru^0. Compared with the pure Ru NPs (Fig. S11), the Ru 3d peak of the N,S-Ti_3C_2 QDs/Ru composites shifted toward a higher binding energy (about 0.2 eV). The result suggests a significant electronic interaction between the Ru NPs and the N,S-Ti_3C_2 QDs support, which improves the HER catalytic activity. The Ti 2p and Ru 3p XPS spectra of N,S-Ti_3C_2 QDs/Ru are shown in Fig. 2i. The binding energy peaks at 465.3, 462.4 and 455.8 eV correspond to Ti—O, Ti—C, and Ti—N bonds, respectively. Additionally, two-component peaks at 460.9 eV and 484.3 eV are observed, which can be attributed to Ru $3p_{3/2}$ for the Ru^0 state, which suggests the existence of metallic Ru in N,S-Ti_3C_2 QDs/Ru [46,47]. The N 1s spectra of N,S-Ti_3C_2 QDs/Ru exhibit typical peaks in 399.2, 398.1 and 397.1 eV, which correspond to pyrrolic-N, Ru-N and Ti-N bonds, respectively (Fig. 2j) [48,49]. The N 1s spectra of N,S-Ti_3C_2 QDs/Ru are shifted toward a lower binding energy than that of N,S-Ti_3C_2 QDs due to the electronic interaction between Ru NPs and the N,S-Ti_3C_2 QDs support. The S 2p spectra for N,S-Ti_3C_2 QDs/Ru can be deconvoluted into four different components, the peaks emerging at 168.0, 163.1, 162.2 and 161.3 eV corresponding to sulfate species, S—C, S-Ru and S-Ti, respectively (Fig. 2k) [37,50]. The Ru-N bond and Ru-S bond found in the N 1s and S 2p XPS spectra unequivocally prove that the Ru is coordinated with both N and S atoms of N,S-Ti_3C_2 QDs support.

The electrocatalytic HER performance of the synthesized materials was examined with the classical three-electrode configuration over wide-pH-range electrolytes. All the measurements are corrected for iR loss. Firstly, we studied the influence of crystallization on the electrocatalytic HER activity of N,S-Ti_3C_2 QDs/Ru in the 0.5 M H_2SO_4 solution. The N,S-Ti_3C_2 QDs/Ru synthesized under 600 °C possesses the lowest overpotential reaching the current density at 10 mA cm^{-2}, and the Tafel slope was minimized (Fig. 3a and Fig. S12). The findings demonstrate that 600 °C is the optimal calcination temperature for synthesizing N,S-Ti_3C_2 QDs/Ru. It is deduced that the low crystallinity reduces the interfacial interaction between the metal Ru and N,S-Ti_3C_2 QDs, and the high crystallinity results in the aggregation of the Ru NPs, which inhibits the electron transport and deactivates the HER activity to some extent. The effect of different Ru loadings on hydrogen precipitation properties was further investigated (Fig. S13). The experimental study revealed that the overpotential was minimized when the $RuCl_3$ aqueous solution

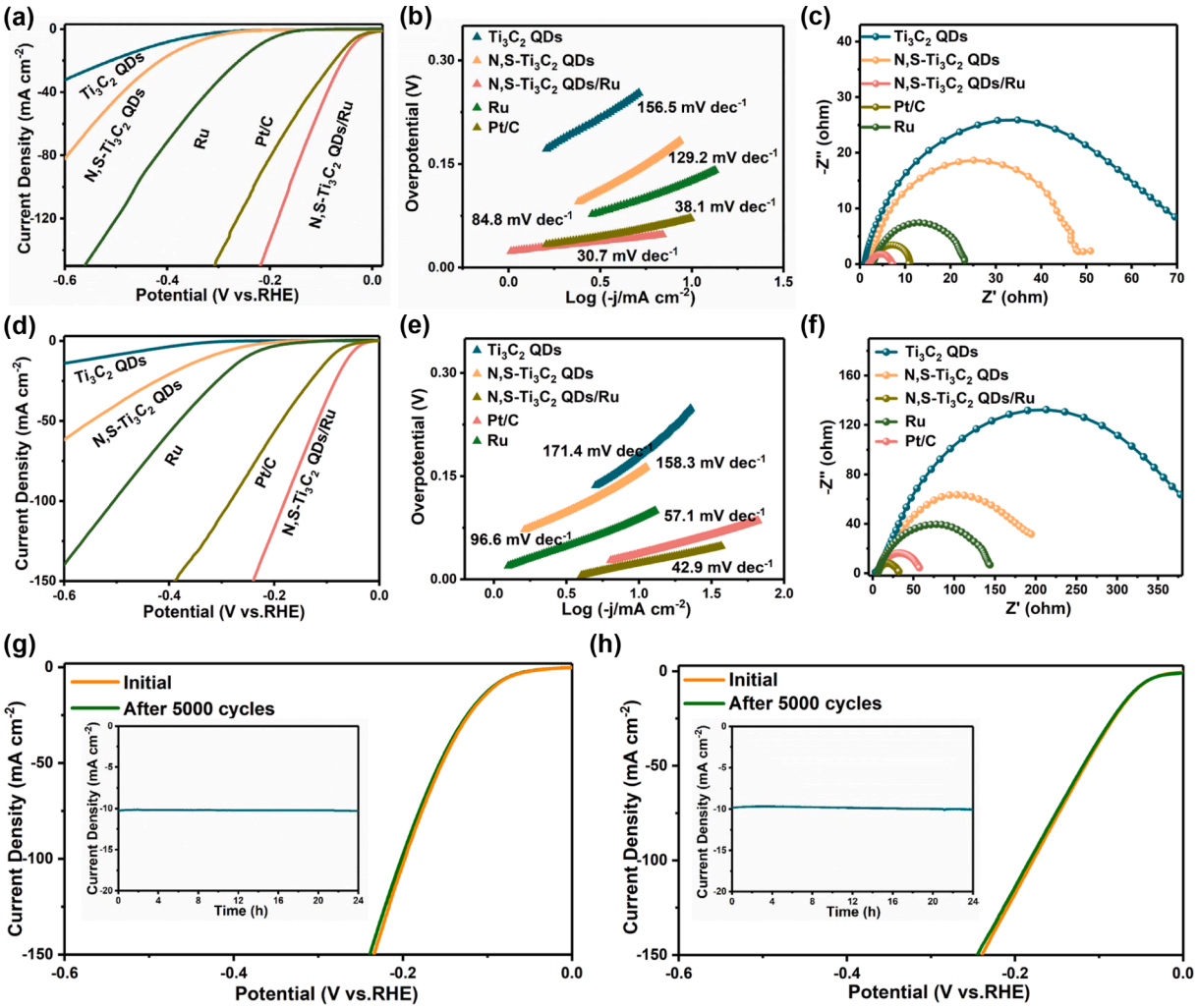

Fig. 4. LSV curves of Ti_3C_2 QDs, N,S-Ti_3C_2 QDs, Ru, 20 wt% Pt/C and N,S-Ti_3C_2 QDs/Ru in: (a) 1 M KOH and (d)1 M PBS electrolytes; Tafel slopes from the LSV curves: (b) 1 M KOH and (e) 1 M PBS; EIS spectra of Ti_3C_2 QDs, N,S-Ti_3C_2 QDs, Ru, 20 wt% Pt/C and N,S-Ti_3C_2 QDs/Ru: in (c) 1 M KOH and (f)1 M PBS; LSV curves for N,S-Ti_3C_2 QDs/Ru before and after 5000 CV cycles. The insets show the current density-time curve for N,S-Ti_3C_2 QDs/Ru: (g) 1 M KOH and (h)1 M PBS solution.

was 5.0 mL, indicating that excessive Ru would agglomerate and reduce the electrocatalytic HER performance. Fig. 3b and Fig. 3c exhibit the LSV curves of metal Ru, N,S-Ti_3C_2 QDs/Ru, Pt/C, N,S-Ti_3C_2 QDs and Ti_3C_2 QDs in 0.5 M H_2SO_4 electrolyte. The Ti_3C_2 QDs show poor HER performance, and the N,S-doping can dramatically boost the catalytic performance of Ti_3C_2 QDs of the HER process. Obviously, N,S-Ti_3C_2 QDs/Ru exhibits a much lower overpotential (28 mV) than both N,S-Ti_3C_2 QDs (345 mV) and Ru (161 mV), suggesting that the excellent electrocatalytic HER performance of N,S-Ti_3C_2 QDs/Ru, which is ascribed to the chemical interactions between Ru and heteroatom doping MXene QDs support. The highly electronegative N and S atoms can form two distinct binding sites with Ru, which contributes to the enhanced HER catalytic performance. To deeply study the reaction kinetics for the synthesized samples during the HER process, the Tafel slopes were computed according to the LSV curves. The smaller Tafel slope suggests a sharp increase in electrocatalytic current density and faster catalytic kinetics. The results reveal that N,S-Ti_3C_2 QDs/Ru exhibits the smallest Tafel slope of 22.4 mV dec^{-1}, which is dramatically smaller than that of the other catalysts, indicating fast HER kinetics (Fig. 3d). It was confirmed that the N,S-Ti_3C_2 QDs/Ru electrocatalyst follows the Volmer-Tafel mechanism based on the Tafel slope value. Remarkably, the HER activity of N,S-Ti_3C_2 QDs/Ru is also comparable to numerous recently reported Ru-based HER electrocatalysts in acidic electrolytes (Fig. 3e and Table S1) [51–57]. The EIS was utilized to analyze the HER internal kinetics of as-prepared catalysts in 0.5 M H_2SO_4 electrolyte (Fig. 3f). Apparently, the N,S-Ti_3C_2 QDs exhibit lower charge-transfer resistance (R_{ct}) than the non-doped Ti_3C_2 MXene QDs, demonstrating that the N and S-doping provide a favorable charge-transfer mechanism. The N,S-Ti_3C_2 QDs/Ru displays the smallest charge transfer resistance (3.6 Ω) than N,S-Ti_3C_2 QDs (82.8 Ω) and commercial Pt/C (5.7 Ω), suggesting that the efficient charge transfer at the interface between N,S-Ti_3C_2 QDs/Ru and electrolyte, thus improving electrocatalytic activity. The result may be associated with the high conductivity of MXene QDs and the electronic interactions between the Ru NPs and the MXene QDs. The mass activity of N,S-Ti_3C_2 QDs/Ru is 6.02 times higher than that of Pt/C under an overpotential of 200 mV, suggesting that the Ru NPs anchored on MXene QDs are capable of providing higher HER mass activity (Fig. 3g). To investigate the ECSA of prepared samples, the C_{dl} was estimated using CV at various scanning speeds (Fig. S14). The results show that the C_{dl} value of N,S-Ti_3C_2 QDs/Ru was 31.8 mF cm^{-2}, which is remarkably larger than that of Ru (11.0 mF cm^{-2}) and N,S-Ti_3C_2 QDs (1.3 mF cm^{-2}), revealing that the higher electrochemically active region and exposed catalytically active sites in N,S-Ti_3C_2 QDs/Ru, which is beneficial to the improving of the HER activity (Fig. 3h). In addition, mass activity plays a critical factor in the economic effectiveness of catalysis and determines the cost of the catalyst. The stability is a primary factor to estimate the HER catalyst performance. Fig. 3i reveals that the final LSV curves of N,S-Ti_3C_2 QDs/

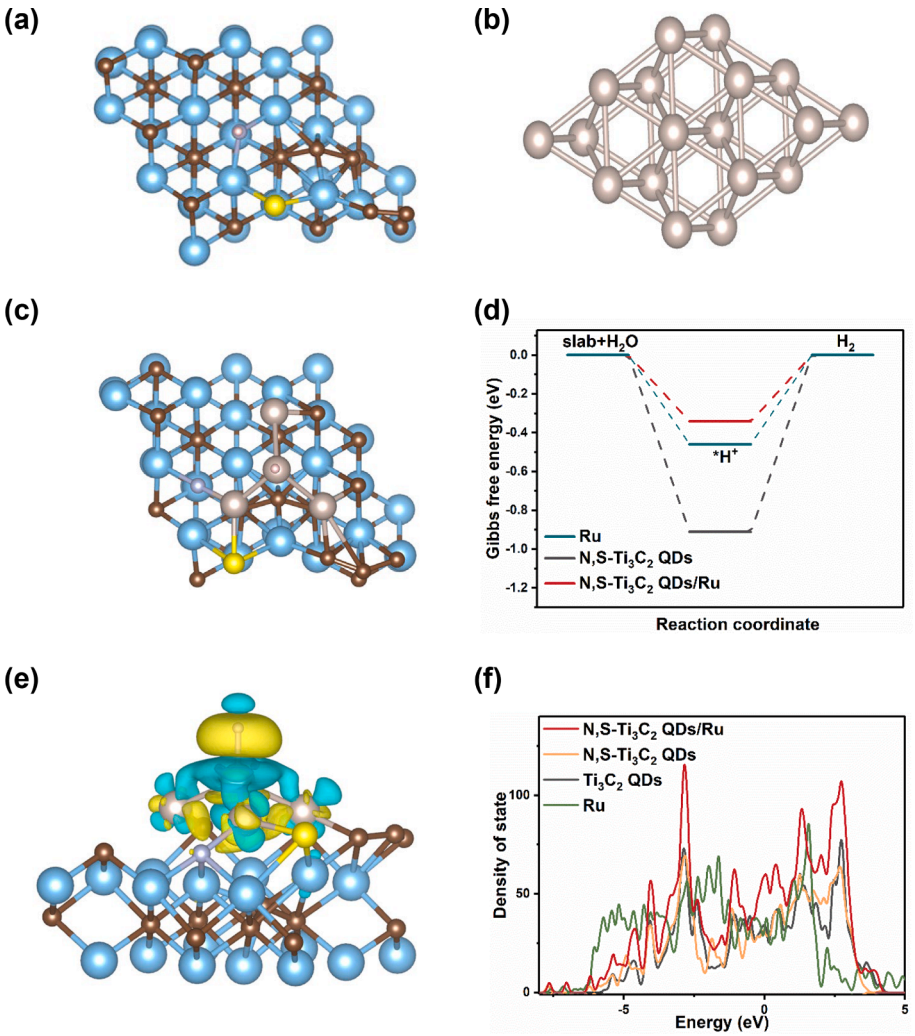

Fig. 5. (a–c) Atomic model of N,S-Ti_3C_2 QDs, Ru and N,S-Ti_3C_2 QDs/Ru; (d) Gibbs hydrogen adsorption free energy for N,S-Ti_3C_2 QDs, Ru and N,S-Ti3C2 QDs/Ru; (e) Charge density difference of N,S-Ti_3C_2 QDs/Ru; (f) Density of states of Ti_3C_2 QDs, N,S-Ti_3C_2 QDs, Ru and N,S-Ti_3C_2 QDs/Ru.

Ru remain virtually unchanged compared to the initial curves after 5000 CV cycles in 0.5 M H_2SO_4 electrolytes, whereas the Pt/C displays a significant negative shift under the same reaction conditions (Fig. S15). Furthermore, the N,S-Ti_3C_2 QDs/Ru catalyst displays superior long-term stability in acidic electrolytes with negligible reduction of HER activity after 24 h of continuous reaction, which further indicates that the Ru is nicely maintained on the N,S-Ti_3C_2 QDs support. We have also employed TEM, HRTEM and XRD techniques to analyze the morphology and crystal structure of the N,S-Ti_3C_2 QDs/Ru catalysts after continuous HER reactions. TEM and HRTEM images of the recycled N,S-Ti_3C_2 QDs/Ru indicate that the Ru NPs are uniformly dispersed without aggregation and the distinct lattice fringes can be observed, which have no impact on the crystallinity (Fig. S16). In addition, the XRD spectra of the recovered N,S-Ti_3C_2 QDs/Ru catalysts are nearly unchanged, suggesting superior structural stability in the HER reaction (Fig. S17). All these findings emphasize the favorable chemical stability and structural robustness of N,S-Ti_3C_2 QDs/Ru toward HER.

In addition to testing in the acidic solution, the HER performance of the prepared N,S-Ti_3C_2 QDs/Ru was further investigated in 1 M KOH and 1 M PBS electrolytes. As illustrated in Fig. 4a, the N,S-Ti_3C_2 QDs/Ru exhibits an excellent activity of 25 mV under a current density of 10 mA cm^{-2} in 1 M KOH electrolyte, which is remarkably lower than that of N, S-Ti_3C_2 QDs (241 mV) and Ru (92 mV). Meanwhile, the N,S-Ti_3C_2 QDs/Ru sample reaches a lower overpotential of 56 mV under a current density of 10 mA cm^{-2} in 1 M PBS electrolyte (Fig. 4d). Additionally, the Tafel slope of synthesized N,S-Ti_3C_2 QDs/Ru is calculated as 30.7 and 42.9 mV·dec^{-1} in 1 M KOH and 1 M PBS electrolyte, which is similar to that of Pt/C, suggesting the faster reaction kinetics (Fig. 4b, e). The smallest overpotential and Tafel slope demonstrate the superior electrocatalytic HER activity of N,S-Ti_3C_2 QDs/Ru in alkaline and neutral electrolyte solutions. Fig. 4 c, f shows that N,S-Ti_3C_2 QDs/Ru possess the lowest charge transfer resistance than that of Ru and N,S-Ti_3C_2 QDs, indicating efficient electron transport and favorable interfacial dynamics in alkaline and neutral electrolyte solutions. The C_{dl} values of N, S-Ti_3C_2 QDs/Ru in alkaline and neutral electrolytes were 36.5 and 17.1 mF cm^{-2}, respectively, which were significantly higher than those of N, S-Ti_3C_2 QDs and Ru, further suggesting that the anchoring of N,S-Ti_3C_2 QDs support to Ru enlarged the electrochemically active region and realized efficient electrocatalytic HER performance (Figs. S18 and S19). Furthermore, the N,S-Ti_3C_2 QDs/Ru catalyst displayed excellent long-term stability over 24 h continuous HER reaction. After 5000 CV cycles, the activity decay for N,S-Ti_3C_2 QDs/Ru was negligible in alkaline and neutral electrolytes (Fig. 4g and h). In comparison, the commercial Pt/C showed a significant decrease in overpotentials and current densities (Figs. S20 and S21), further confirming the N,S-Ti_3C_2 QDs/Ru possesses superior electrochemical HER stability than the commercial Pt/C. The Ru dissolution behavior of N,S-Ti_3C_2 QDs/Ru was systematically investigated using ICP-OES. The experimental results show that N, S-Ti_3C_2 QDs/Ru exhibited only a trace amount of Ru dissolution in 0.5 M H_2SO_4, 1 M KOH, and 1 M PBS solutions (Fig. S22), confirming the

effective anchoring effect of the N,S-Ti_3C_2 QDs carriers on the Ru NPs, which significantly inhibited the dissolution loss of the active component Ru during the electrocatalytic process. In summary, we can conclude that the designed N,S-Ti_3C_2 QDs/Ru is an efficient and robust HER electrocatalyst under different pH values.

DFT calculations are utilized to study the electronic interaction between metal Ru and the N,S-Ti_3C_2 QDs support, and get more insight into the fundamental mechanism of the N,S-Ti_3C_2 QDs/Ru catalyst for enhancing the HER activity. In this work, we develop corresponding atomic models for N,S-Ti_3C_2 QDs, Ru and N,S-Ti_3C_2 QDs/Ru in DFT simulation (Fig. 5a–c). In which, blue, brown, yellow, purple and light gold colors symbolize Ti, C, S, N and Ru atoms, respectively. Generally speaking, the ΔGH*of the electrocatalyst surface is a critical factor for investigating the HER catalytic activity. As illustrated in Fig. 5d, the N,S-Ti_3C_2 QDs and Ru catalysts exhibit highly negative ΔGH* values of −0.96 and −0.43 eV, suggesting that the stronger H adsorption behavior of these catalysts, resulting in higher energy barriers to H_2 formation and desorption. Surprisingly, N,S-Ti_3C_2 QDs/Ru reaches the optimal ΔGH* value at −0.24 eV, demonstrating that the more beneficial H adsorption–desorption behavior subsequently improves HER catalytic performance for N,S-Ti_3C_2 QDs/Ru. The charge density difference shows a strong charge redistribution upon Ru NPs loading N,S-Ti_3C_2 QDs (Fig. 5e), which dramatically increases the interior electron concentration within the composite system. Moreover, the charge density difference confirms the efficient electron transfer from Ru NPs to the surrounding N and S atoms and Ti_3C_2 QDs support, thus diminishing the Ru-H bond and boosting the HER catalytic performance [52]. The total density of states (TDOS) for Ti_3C_2 QDs, N,S-Ti_3C_2 QDs, Ru and N,S-Ti_3C_2 QDs/Ru suggests that all the systems exhibit metallic characteristics and high electronic conductivity, which is conducive to the electrocatalytic HER (Fig. 5f). Among them, N,S-Ti_3C_2 QDs/Ru presents the highest carrier density around the Fermi level, which contributes to the better activation and electron transport of Ru on the surface of N,S-Ti_3C_2 QDs/Ru, resulting in the enhanced HER [58]. Therefore, all DFT calculations confirmed that the modification of Ru onto the N,S-doped MXene QDs carriers effectively adjusts the electronic structure of Ru, achieving optimal ΔGH*, therefore dramatically improving the HER activity.

4. Conclusion

In summary, we have successfully prepared heteroatom N and S Co-doped Ti_3C_2 MXene QDs as a robust carrier for anchoring Ru NPs for efficient electrocatalytic HER. In previous studies, the application of MXene materials in electrocatalysis was mostly confined to their two-dimensional lamellar structures, whereas this study significantly increased the specific surface area and the density of edge active sites of MXene by quantum dotting and combined with heteroatom doping. The optimal N,S-Ti_3C_2 QDs/Ru catalyst exhibited superior HER performance and stability over a wide pH range, which is comparable to that of Pt/C catalysts. Additionally, DFT calculations revealed that the interaction between Ru and N,S-Ti_3C_2 QDs effectively adjusted the electronic structure of the active center Ru, contributed to promoting the dissociation of water, and optimized the adsorption and desorption of H_2, thereby synergistically facilitating the improvement of the HER performance. This work demonstrates the potential of MXene quantum dots, as a platform in the design of HER electrocatalysts, stimulates future research on other MXene QDs-supported metal catalysts, and provides a universal and prospective strategy to rationally design and prepare efficient and low-cost catalysts for electrocatalysis and energy applications.

CRediT authorship contribution statement

Lan Ding: Writing – original draft. **Jing Xu:** Data curation. **Zeyu Zhang:** Formal analysis. **Kezhen Qi:** Writing – review & editing. **Ge Jin:** Formal analysis.

Declaration of competing interest

The authors declare that they have no known competing financial interests or personal relationships that could have appeared to influence the work reported in this paper.

Acknowledgments

This research was supported by the Yunnan Provincial Science and Technology Plan Projects (202305AF150116, 202301AT070027) and National Natural Science Foundation of China (22268003).

Appendix A. Supplementary data

Supplementary data to this article can be found online at https://doi.org/10.1016/j.jcis.2025.03.034.

Data availability

No data was used for the research described in the article.

References

[1] C.X. Wang, W.X. Guo, T.L. Chen, W.Y. Lu, Z.Y. Song, C.C. Yan, Y. Feng, F.M. Gao, X.N. Zhang, Y.P. Rao, L.T. Qian, S.M. Xu, G.Y. Huang, Y. Zheng, W. Yan, J.J. Zhang, Advanced noble-metal/transition-metal/metal-free electrocatalysts for hydrogen evolution reaction in water-electrolysis for hydrogen production, Coord. Chem. Rev. 514 (2024) 215899.
[2] Y. Cheng, H.Y. Chen, L.F. Zhang, X.N. Xu, H.L. Cheng, C.L. Yan, T. Qian, Evolution of grain boundaries promoted hydrogen production for industrial-grade current density, Adv. Mater. 36 (2024) 2313156.
[3] L.J. Yang, H. Li, Y. Yu, Y. Wu, L. Zhang, Assembled 3D MOF on 2D nanosheets for self-boosting catalytic synthesis of N-doped carbon nanotube encapsulated metallic Co electrocatalysts for overall water splitting, Appl. Catal. B 271 (2020) 118939.
[4] Z.H. Wang, Y.X. Bai, Y.P. Li, K.X. Tao, M. Simayi, Y.C. Li, Z.H. Chen, Y.J. Sun, X. Chen, X.L. Pang, Y.H. Ma, K.Z. Qi, $Bi_2O_2CO_3$/red phosphorus S-scheme heterojunction for H_2 evolution and Cr(VI) reduction, J. Colloid Interface Sci. 609 (2022) 320–329.
[5] X.Y. Zhao, J.J. Wang, J.Z. Kang, X.M. Wang, H. Yu, C.F. Du, Ni nanoparticles anchoring on vacuum treated $Mo_2TiC_2T_x$ MXene for enhanced hydrogen evolution activity, Chin. J. Struct. Chem. 42 (2023) 100159.
[6] S.J. Wan, W. Wang, B. Cheng, G.Q. Luo, Q. Shen, J.G. Yu, J.J. Zhang, S.W. Cao, L. M. Zhang, A superlattice interface and S-scheme heterojunction for ultrafast charge separation and transfer in photocatalytic H_2 evolution, Nat. Commun. 15 (2024) 9612.
[7] R.C. Li, F.Y. Liu, Q.Q. Xu, J.L. Yu, K.Z. Qi, Manipulating heterointerface to boost formation and desorption of intermediates for highly efficient alkaline hydrogen evolution, J. Colloid Interface Sci. 671 (2024) 469–476.
[8] X.Q. Gao, Y.T. Chen, Y.J. Wang, L.Y. Zhao, X.Y. Zhao, J. Du, H.X. Wu, A.B. Chen, Next-generation green hydrogen: progress and perspective from electricity, catalyst to electrolyte in electrocatalytic water splitting, Nano-Micro Lett. 16 (2024) 237.
[9] H.B. Yang, D.W. Ma, Y. Li, Q.H. Zhao, F. Pan, S.S. Zheng, Z.R. Lou, Mo doped Ru-based cluster to promote alkaline hydrogen evolution with ultra-low Ru loading, Chin. J. Struct. Chem. 42 (2023) 100031.
[10] L. Quan, H. Jiang, G.L. Mei, Y.J. Sun, B. You, Bifunctional electrocatalysts for overall and hybrid water splitting, Chem. Rev. 124 (2024) 3694–3812.
[11] H.H. Hu, Z.R. Zhang, Y.W. Zhang, T.J. Thomas, H.Y. Du, K.K. Huang, J.P. Attfield, M.H. Yang, An ultra-low Pt metal nitride electrocatalyst for sustainable seawater hydrogen production, Energ. Environ. Sci. 16 (2023) 4584–4592.
[12] Y.M. Da, R. Jiang, Z.L. Tian, G.W. Chen, Y.K. Xiao, J.F. Zhang, S.B. Xi, Y.D. Deng, W. Chen, X.P. Han, W.B. Hu, Development of a novel Pt_3V alloy electrocatalyst for highly efficient and durable industrial hydrogen evolution reaction in acid environment, Adv. Energy Mater. 13 (2023) 2300127.
[13] H.F. Yuan, D. Jiang, Z.M. Li, X.Y. Liu, Z.F. Tang, X.H. Zhang, L.L. Zhao, M. Huang, H. Liu, K.P. Song, W.J. Zhou, Laser synthesis of PtMo single-atom alloy electrode for ultralow voltage hydrogen generation, Adv. Mater. 36 (2024) 2305375.
[14] Z. Xu, J. Zhu, Z. Shu, Y. Xia, R.X. Chen, S.Q. Chen, Y. Wang, L. Zeng, J.C. Wang, Y. Q. Cai, S. Chen, F.Q. Huang, H.L. Wang, Phosphorus-induced anti-growth of ruthenium clusters-single atoms for ultra-stable hydrogen evolution over 100,000 cycles, Joule 8 (2024) 1790–1803.
[15] W.Y. Gou, Y.C. Wang, M.K. Zhang, X.H. Tan, Y.Y. Ma, Y.Q. Qu, A review on fundamentals for designing stable ruthenium-based catalysts for the hydrogen and oxygen evolution reactions, Chin. J. Catal. 60 (2024) 68–106.
[16] Y.P. Zhu, K. Fan, C.S. Hsu, G. Chen, C.S. Chen, T.C. Liu, Z.Z. Lin, S.X. She, L.Q. Li, H.M. Zhou, Y. Zhu, H.M. Chen, H.T. Huang, Supported ruthenium single-atom and clustered catalysts outperform benchmark Pt for alkaline hydrogen evolution, Adv. Mater. 35 (2023) 2301133.

[17] Y.B. Kuang, F.L. Yang, L.G. Feng, Advancements in ruthenium (Ru)-based heterostructure catalysts: overcoming bottlenecks in catalysis for hydrogen evolution reaction, Adv. Energy Mater. 14 (2024) 2402043.
[18] Y. Chen, Y.D. Liu, L. Li, T. Sakthivel, Z.X. Guo, Z.F. Dai, Intensifying the supported ruthenium metallic bond to boost the interfacial hydrogen spillover toward pH-universal hydrogen evolution catalysis, Adv. Funct. Mater. 34 (2024) 2401452.
[19] X.J. Liu, S.C. Wei, S.Y. Cao, Y.G. Zhang, W. Xue, Y.J. Wang, G.H. Liu, J.D. Li, Lattice strain with stabilized oxygen vacancies boosts ceria for robust alkaline hydrogen evolution outperforming benchmark Pt, Adv. Mater. 36 (2024) 2405970.
[20] Y.Z. Wu, L. Wang, T. Bo, Z.F. Chai, J.K. Gibson, W.Q. Shi, Boosting hydrogen evolution in neutral medium by accelerating water dissociation with Ru clusters loaded on Mo_2CT_x MXene, Adv. Funct. Mater. 33 (2023) 2214375.
[21] J.H. Su, K. Shi, B.C. Liu, Z.C. Xi, J.C. Yu, X. Xu, P. Jing, R. Gao, J. Zhang, Engineering the metal-support interaction and oxygen vacancies on Ru@P-Fe/Fe_3O_4 nanorods for synergetic enhanced electrocatalytic nitrate-to-ammonia conversion, Adv. Funct. Mater. 34 (2024) 2401194.
[22] C.C. Zhang, L.X. Sun, Y.F. Ouyang, F. Xu, Y.J. Zou, H.L. Chu, K.X. Zhang, B. Li, H. G. Pan, Improved electrochemical water splitting by RuNi nanoparticles supported on rGO@mesoporous N-doped carbon nanosheets, J. Alloy. Compd. 937 (2023) 168334.
[23] Z. Liu, X.D. Yang, G.Z. Hu, L.G. Feng, Ru nanoclusters coupled on Co/N-doped carbon nanotubes efficiently catalyzed the hydrogen evolution reaction, ACS Sustain. Chem. Eng. 8 (2020) 9136–9144.
[24] Z.L. Liu, B.Q. Li, Y.J. Feng, D.C. Jia, C.C. Li, Y. Zhou, N-doped sp^2/sp^3 carbon derived from carbon dots to boost the performance of ruthenium for efficient hydrogen evolution reaction, Small Methods 6 (2022) 2200637.
[25] T. Cui, X.J. Zhai, L.L. Guo, J.Q. Chi, Y. Zhang, J.W. Zhu, X.M. Sun, L. Wang, Controllable synthesis of a self-assembled ultralow Ru, Ni-doped Fe_2O_3 lily as a bifunctional electrocatalyst for large-current-density alkaline seawater electrolysis, Chin. J. Catal. 43 (2022) 2202–2211.
[26] A.H. Feng, Y. Yu, Y. Wang, F. Jiang, Y. Yu, L. Mi, L.X. Song, Two-dimensional MXene Ti_3C_2 produced by exfoliation of Ti_3AlC_2, Mater. Des. 114 (2017) 161–166.
[27] W.C. Bi, G.H. Gao, C. Li, G.M. Wu, G.Z. Cao, Synthesis, properties, and applications of MXenes and their composites for electrical energy storage, Prog. Mater Sci. 142 (2024) 101227.
[28] Y. Guo, Z.G. Du, Z.J. Cao, B. Li, S.B. Yang, MXene derivatives for energy storage and conversions, Small Methods 7 (2023) 2201559.
[29] Q. Xue, H.J. Zhang, M.S. Zhu, Z.X. Pei, H.F. Li, Z.F. Wang, Y. Huang, Y. Huang, Q. H. Deng, J. Zhou, S.Y. Du, Q. Huang, C.Y. Zhi, Photoluminescent Ti_3C_2 MXene quantum dots for multicolor cellular imaging, Adv. Mater. 29 (2017) 1604847.
[30] C. Guan, X.Y. Yue, J.J. Fan, Q.J. Xiang, MXene quantum dots of Ti_3C_2: properties, synthesis, and energy-related applications, Chin. J. Catal. 43 (2022) 2484–2499.
[31] W. Jiang, X.L. Zou, H.D. Du, L. Gan, C.J. Xu, F.Y. Kang, W.H. Duan, J. Li, Universal descriptor for large-scale screening of high-performance MXene-based materials for energy storage and conversion, Chem. Mater. 30 (2018) 2687–2693.
[32] L. Meng, L.K. Yan, F. Viñes, F. Illas, Effect of terminations on the hydrogen evolution reaction mechanism on Ti_3C_2 MXene, J. Mater. Chem. A 11 (2023) 6886–6900.
[33] Z.P. Zeng, Y.B. Yan, J. Chen, P. Zan, Q.H. Tian, P. Chen, Boosting the photocatalytic ability of Cu_2O nanowires for CO_2 conversion by MXene quantum dots, Adv. Funct. Mater. 29 (2019) 1806500.
[34] P. Wang, D.Y. Zhao, X.B. Hui, Z. Qian, P. Zhang, Y.Y. Ren, Y. Lin, Z.W. Zhang, L. W. Yin, Bifunctional catalytic activity guided by rich crystal defects in Ti_3C_2 MXene quantum dot clusters for Li-O_2 batteries, Adv. Energy Mater. 11 (2021) 2003069.
[35] Z.J. Qi, Y. Zhou, R.N. Guan, Y.S. Fu, J.B. Baek, Tuning the coordination environment of carbon-based single-atom catalysts via doping with multiple heteroatoms and their applications in electrocatalysis, Adv. Mater. 35 (2023) 2210575.
[36] X.Y. Cheng, C.H. Mao, J.Y. Tian, M.Q. Xia, L.J. Yang, X.Z. Wang, Q. Wu, Z. Hu, Correlation between heteroatom coordination and hydrogen evolution for single-site Pt on carbon-based nanocages, Angew. Chem. Int. Ed. 63 (2024) e202401304.
[37] W.J. Lin, Y.R. Lu, W. Peng, M. Luo, T.S. Chan, Y.W. Tan, Atomic bridging modulation of Ir-N, S co-doped MXene for accelerating hydrogen evolution, J. Mater. Chem. A 10 (2022) 9878–9885.
[38] J.N. Feng, W.D. Liu, C. Shi, C.Y. Zhang, X.X. Zhao, T.Y. Wang, S.Q. Chen, Q. Li, J. J. Song, Enabling fast diffusion/conversion kinetics by thiourea-induced wrinkled N, S co-doped functional MXene for lithium-sulfur battery, Energy Storage Mater. 67 (2024) 103328.
[39] B.X. Zhang, Y. Wang, Z.Q. Wang, G.Q. Tan, T. Liu, S.J. Feng, Y.Z. Tan, W.L. Liu, Q. Yang, Y. Liu, A. Xia, H.J. Ren, Y.T. Wu, Surface plasmon resonance effects of Ti_3C_2 MXene for degradation of antibiotics under full spectrum, Appl. Catal. B 339 (2023) 123132.
[40] B.F. Zhang, J.W. Yang, Y.B. Mu, X.Y. Ji, Y.D. Cai, N. Jiang, S.H. Xie, Q.H. Qian, F. D. Liu, W. Tan, L. Dong, Fabrication of highly dispersed Ru catalysts on CeO_2 for efficient C_3H_6 oxidation, Environ. Sci. Tech. 58 (2024) 19533–19544.
[41] Y.B. Li, C.Q. Cheng, S.H. Han, Y.M. Huang, X.W. Du, B. Zhang, Y.F. Yu, Electrocatalytic reduction of low-concentration nitric oxide into ammonia over Ru nanosheets, ACS Energy Lett. 7 (2022) 1187–1194.
[42] L. Huang, L.X. Ma, J. Yang, J.H. Kang, Y. Chen, J.Q. Yan, Y.P. Fang, D. Li, R. B. Jiang, Electron donation from carbon support enhances the activity and stability of ultrasmall ruthenium dioxide nanoparticles in acidic oxygen evolution reaction, J. Colloid Interface Sci. 686 (2025) 438–447.
[43] Y. Sun, P.P. Li, Y. Zhu, X.H. Zhu, Y.Y. Zhang, M.L. Liu, Y. Liu, In situ growth of TiO_2 nanowires on Ti_3C_2 MXenes nanosheets as highly sensitive luminol electrochemiluminescent nanoplatform for glucose detection in fruits, sweat and serum samples, Biosens. Bioelectron. 194 (2021) 113600.
[44] Z.Z. Wei, Z.J. Zhao, J. Wang, Q. Zhou, C.X. Zhao, Z.H. Yao, J.G. Wang, Oxygen-deficient TiO_2 and carbon coupling synergistically boost the activity of Ru nanoparticles for the alkaline hydrogen evolution reaction, J. Mater. Chem. A 9 (2021) 10160–10168.
[45] C.L. Xu, M. Ming, Q. Wang, C. Yang, G.Y. Fan, Y. Wang, D.J. Gao, J. Bi, Y. Zhang, Facile synthesis of effective Ru nanoparticles on carbon by adsorption-low temperature pyrolysis strategy for hydrogen evolution, J. Mater. Chem. A 6 (2018) 14380–14386.
[46] S.Y. Nong, W.J. Dong, J.W. Yin, B.W. Dong, Y. Lu, X.T. Yuan, X. Wang, K.J. Bu, M. Y. Chen, S.D. Jiang, L.M. Liu, M.L. Sui, F.Q. Huang, Well-dispersed ruthenium in mesoporous crystal TiO_2 as an advanced electrocatalyst for hydrogen evolution reaction, J. Am. Chem. Soc. 140 (2018) 5719–5727.
[47] Y.Z. Li, J. Abbott, Y.C. Sun, J.M. Sun, Y.C. Du, X.J. Han, G. Wu, P. Xu, Ru nanoassembly catalysts for hydrogen evolution and oxidation reactions in electrolytes at various pH values, Appl. Catal. B 258 (2019) 117952.
[48] H.Y. Xu, R.X. Zheng, D.Y. Du, L.F. Ren, X.J. Wen, X.X. Wang, G.L. Tian, C.Z. Shu, Adjusting the 3d orbital occupation of Ti in Ti_3C_2 MXene via nitrogen doping to boost oxygen electrode reactions in Li-O_2 battery, Small 19 (2023) 2206611.
[49] Y.Z. Song, Z.T. Sun, Z.D. Fan, W.L. Cai, Y.L. Shao, G. Sheng, M.L. Wang, L.X. Song, Z.F. Liu, Q. Zhang, J.Y. Sun, Rational design of porous nitrogen-doped Ti_3C_2 MXene as a multifunctional electrocatalyst for Li-S chemistry, Nano Energy 70 (2020) 104555.
[50] Y.L. An, Y. Tian, C.K. Liu, S.L. Xiong, J.K. Feng, Y.T. Qian, Rational design of sulfur-doped three-dimensional $Ti_3C_2T_x$ MXene/ZnS heterostructure as multifunctional protective layer for dendrite-free zinc-ion batteries, ACS Nano 15 (2021) 15259–15273.
[51] C.D. Si, Z.X. Wu, J. Wang, Z.H. Lu, X.F. Xu, J.S. Li, Enhanced the hydrogen evolution performance by ruthenium nanoparticles doped into cobalt phosphide nanocages, ACS Sustain. Chem. Eng. 7 (2019) 9737–9742.
[52] V. Ramalingam, P. Varadhan, H.C. Fu, H. Kim, D.L. Zhang, S.M. Chen, L. Song, D. Ma, Y. Wang, H.N. Alshareef, J.H. He, Heteroatom-mediated interactions between ruthenium single atoms and an MXene support for efficient hydrogen evolution, Adv. Mater. 31 (2019) 1903841.
[53] X.F. Ma, H. Xiao, Y. Gao, M. Zhao, L. Zhang, J.M. Zhang, J.F. Jia, H.S. Wu, Enhancement of pore confinement caused by the mosaic structure on Ru nanoparticles for pH-universal hydrogen evolution reaction, J. Mater. Chem. A 11 (2023) 3524–3534.
[54] D.K. Zhao, Z.L. Li, X.L. Yu, W. Zhou, Q.K. Wu, Y. Luo, N. Wang, A.M. Liu, L.G. Li, S. W. Chen, Ru decorated Co nanoparticles supported by N-doped carbon sheet implements Pt-like hydrogen evolution performance in wide pH range, Chem. Eng. J. 450 (2022) 138254.
[55] H.B. Zhang, W. Zhou, X.F. Lu, T. Chen, X.W. Lou, Implanting isolated Ru atoms into edge-rich carbon matrix for efficient electrocatalytic hydrogen evolution, Adv. Energy Mater. 10 (2020) 2000882.
[56] D. Yoon, J. Lee, B. Seo, B. Kim, H. Baik, S. Hoon Joo, K. Lee, Cactus-like hollow Cu_{2-S}@Ru Nanoplates as excellent and robust electrocatalysts for the alkaline hydrogen evolution reaction, Small 13 (2017) 1700052.
[57] W. Xu, H.J. Xie, F.Y. Cao, S.S. Ran, Y.H. Duan, B. Li, L. Wang, Enhanced interaction between Ru nanoparticles and N, C-modified mesoporous TiO_2 for efficient electrocatalytic hydrogen evolution at all pH values, J. Mater. Chem. A 10 (2022) 23751–23759.
[58] W. Peng, J.H. Han, Y.R. Lu, M. Luo, T.S. Chan, M. Peng, Y.W. Tan, A general strategy for engineering single-metal sites on 3D porous N, P Co-doped $Ti_3C_2T_X$ MXene, ACS Nano 16 (2022) 4116–4125.